City Research Online

City, University of London Institutional Repository

Citation: Bruecker, C. ORCID: 0000-0001-5834-3020 and du Puits, R. (2020). Fluctuations of the wall shear stress vector in a large-scale natural convection cell. AIP Advances,

This is the accepted version of the paper.

This version of the publication may differ from the final published version.

Fluctuations of the wall shear stress vector in a large-scale natural convection cell

R. du Puits[1], C. Bruecker,[2,a)].

[1] *Institute of Thermodynamics and Fluid Mechanics, Technische Universitaet Ilmenau, 98684 Ilmenau, Germany*

[2] *School of Mathematics, Computer Science and Engineering, City, University of London, London EC1V 0HB, UK*

We report first experimental data of the wall shear stress in turbulent air flow in a large-scale Rayleigh-Bénard experiment. Using a novel, nature-inspired measurement concept (Bruecker and Mikulich 2017, PLoS ONE 12, e0179253), we measured the mean and fluctuating part of the two components of the wall shear stress vector at the heated bottom plate at a Rayleigh number Ra=1.58e10 and a Prandtl number Pr=0.7. The total sampling period of 1,5 hours allowed to capture the dynamics of the magnitude and the orientation of the vector over several orders of characteristic time-scales of the large-scale circulation. We found the amplitude of short-term (turbulent) fluctuations to be following a highly skewed Weibull distribution, while the long-term fluctuations are dominated by the modulation effect of a quasi-regular angular precession of the outer flow around a constant mean, the time-scale of which is coupled to the characteristic eddy turn-over time of the global recirculation roll. Events of instantaneous negative streamwise wall shear occur when rapid twisting of the local flow happens. A mechanical model is used to explain the precession by tilting the spin moment of the large circulation roll and conservation of angular momentum. A slow angular drift of the mean orientation is observed in a phase of considerable weakening of mean wind magnitude.

a) corresponding author: christoph.bruecker@city.ac.uk

I. INTRODUCTION

Since Ludwig Prandtl's pioneering work, we know that the local heat transport at a surface with a temperature differing from that of the surrounded fluid is linked to the local momentum transport across the fluid layer close to the surface[1]. Measurements of the local wall shear stress (WSS) may, therefore, contribute to a better understanding of the convective heat transfer process. However, that kind of data reflecting the dynamics of the local heat/momentum transport is rare, and to our knowledge, the present work is the first one providing measurement data of the instantaneous two-dimensional (2-D) vector of the local WSS in thermal convection.

Following Prandtl's idea, Ludwieg carried out a first analysis of the relation between the heat and momentum transport in thermal convection. Unfortunately, he did not have the appropriate metrology, and he could obtain only the time-averaged WSS from measurements of the profile of the velocity parallel to the wall[2]. For large-scale air convection studies such as in the so-called "Barrel of Ilmenau" (BOI), the existing data base is still limited to mean velocity profile measurements from which only a single component of the mean WSS could be derived. Due to the lack of sufficiently sensitive sensors of the WSS, the current status quo in such data knowledge is therefore solely available from Direct Numerical Simulations (DNS). Such simulations provide the local WSS vector information in time, but usually for a limited simulation period of only a few tens of minutes. First simulation data, published by Scheel and Schumacher[3] show the existence of singularities in the wall shear stress vector field similar as those reported in Bruecker[4]. These singularities are considered as footprints of large eruptions of fluid parcels from the wall, who significantly affect the heat transport[5]. It is, therefore, the authors' conclusion that information on the magnitude and the angle of the WSS vector as well as information on its temporal behavior are crucial to understand the local momentum and heat transport processes at the wall.

In order to measure the instantaneous WSS in low-speed air flows, Bruecker and Mikulich developed a novel sensor, which was particularly designed to be used in large-scale convection air flows such as in the Barrel of Ilmenau[6]. As the authors of the paper report, the sensitivity and the dynamic response of the sensor, which is based on a nature-grown Dandelion pappus, were sufficiently good to resolve the dynamics of the very small WSS in thermal convection in air. The present work reports the first application of this sensor in a large-scale convection experiment in the BOI. It addresses the hitherto unknown dynamics of the WSS by simultaneously measuring the magnitude and the direction of the WSS vector. The results display the behavior of the modulation of the local WSS by the outer main wind and give insight into the statistics and dynamics of the turbulent boundary layer.

The paper is organized as follows: In Section 2, we describe the essentials of the measurement technology as well as the convection experiment wherein the sensor has been applied. Section 3 contains the results of our measurements and in Section 4, we summarize our discussion.

II. EXPERIMENTAL SET-UP AND MEASUREMENT TECHNIQUE

A. The large-scale Rayleigh-Bénard experiment ”Barrel of Ilmenau”

The WSS measurements were carried out in the so-called ”Barrel of Ilmenau (BOI)” a Rayleigh-Bénard (RB) experiment using air ($Pr = 0.7$) as working fluid (see Fig. 1) and with the sensor mounted at the center of the bottom plate. The BOI consists of a virtually adiabatic container of cylindrical shape with an inner diameter of $D = 7.15$ m. A heating plate at the lower side releases the heat to the air layer, and a cooling plate at the upper side removes it. Both plates are carefully levelled perpendicular to the vector of gravity with an uncertainty of less than 0.15 degrees. The thickness of the air layer H can be varied continuously between $0.15\text{ m} < H < 6.30\text{ m}$ by moving the cooling plate up and down. The temperature of both plates can be set to values between $20°\text{C} < T_h < 80°\text{C}$ (heating plate) and $10°\text{C} <$

$T_c < 30°C$ (cooling plate). Due to the specific design of both plates (for more details see du Puits et al.[7]), the temperature at their surfaces is very uniform and the deviation does not exceed 1.5 % of the total temperature drop $\Delta T = T_h - T_c$ across the air layer.

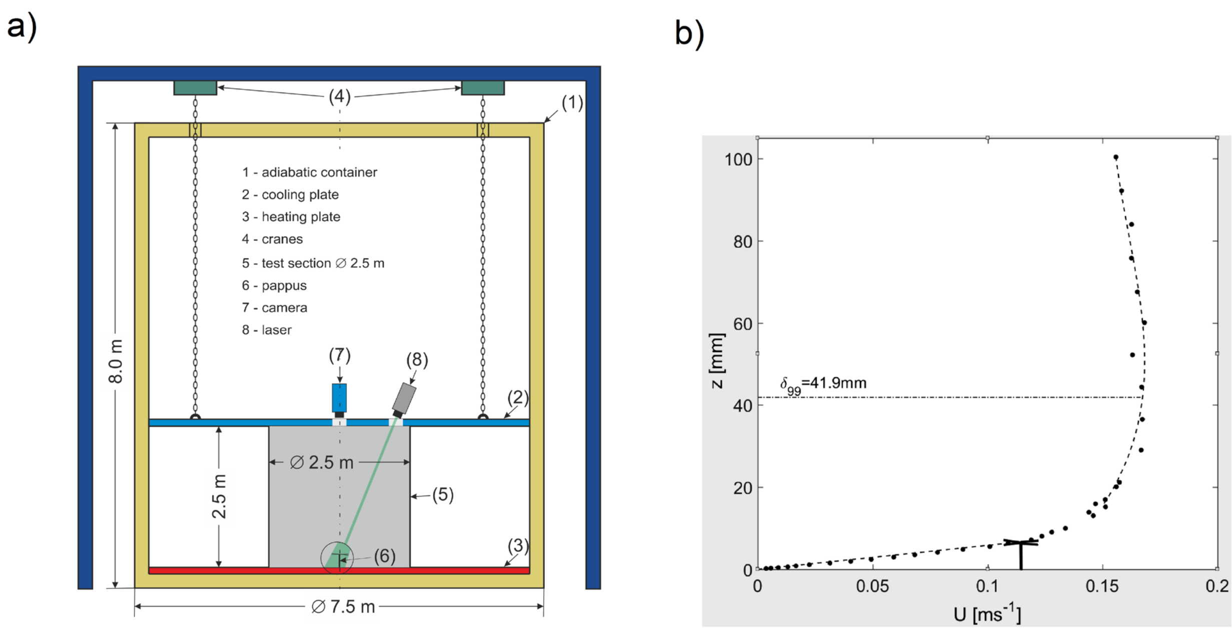

Figure 1a: Sketch of the large-scale Rayleigh-Bénard experiment "Barrel of Ilmenau" with the smaller inset of $D = 2.5\ m$. The origin of a Cartesian coordinate system is fixed with the center of the bottom wall (the location of the wall shear stress sensor) in the x, y plane and the z axis pointing normal to the wall towards the top plate. Figure 1b: Mean velocity profile in the boundary layer of the BOI7 at the center of the cell. The plot shows the magnitude of the velocity vector at the centerline in different planes z parallel to the surface of the wall. Inserted is a true-scale sketch of the sensor with its head at z_0=7 mm, illustrating that it is fully surrounded by the linear part of the velocity profile

The variation of the surface temperature over the time is even smaller and remains below ± 0.02 K. The sidewall of the convection cell is equipped with an active compensation heating system that efficiently prevents a heat exchange between the interior of the RB cell and the environment. Glass windows in the top plate allow the optical access to the interior of the test section for the illumination and for taking recordings. For our measurements we used a smaller inset of diameter $D = 2.5$ m and height $H = 2.5$ m that was placed within the large-size test section (see also Fig. 1). The temperature at the bottom heating plate was set to T_h = 25°C and at the top cooling plate to T_c = 15°C , thus providing a temperature difference of $\Delta T = 10$ K. The Rayleigh number $Ra = (\beta g \Delta T H^3)/(\nu\kappa)$ under these conditions is $Ra = 1.58 \cdot 10^{10}$, with the thermal expansion coefficient β = 3.421e-3 K^{-1}, the gravitational acceleration g= 9.81 ms^{-2}, the kinematic viscosity ν = 1.532e-5 m^2s^{-1} at 20°, and the thermal diffusivity κ = 2.163e-5 m^2s^{-1}. The particular benefit of the inset configuration is the fact that the vertical temperature distribution inside and outside the inset equals, therefore the sidewall can be considered as fully adiabatic. The characteristic timescale of the flow in the test section is the so-called free-fall time unit, defined as $T_f = \sqrt{\beta g \Delta T H}$, which is about $T_f = 2.7$ s for the current configuration. Another timescale is the characteristic eddy turnover time T_e of the large circulation cell (LSC) in form of a single recirculation roll, which is calculated from the mean wind $U = 0.15\ \mathrm{ms}^{-1}$ and the circumference of the cell to about $T_e = 50$ s.

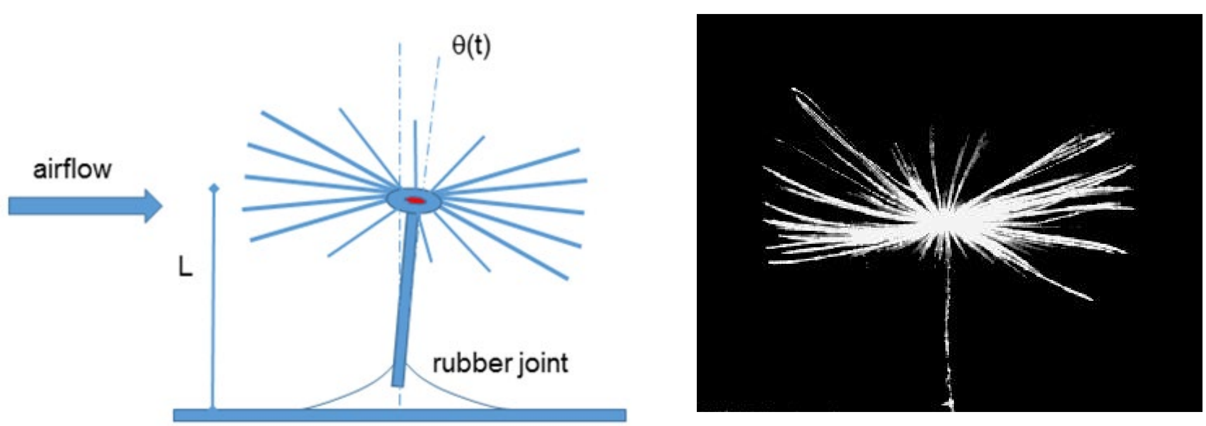

Figure 2: Principle of the measurement concept using a wall-mounted cantilever beam with a pappus head (left). Pictures of the pappus sensor fixated with the stem in the flexible membrane at the bottom plate of the BOI (right).

The wall shear stress sensor

The sensor including its calibration in the BOI is described in detail in Bruecker and Mikulich[6]. It follows the principle of an indirect WSS measurement by calculating the near-wall velocity gradient from the wall-parallel velocity at a given (short) distance from the wall. It is based on the flow-induced deflection of an elastically-mounted cantilever beam (inverted pendulum) that is built at his head from a pappus of micro-hairs (nature-grown Dandelion pappus) (Fig. 2). To maximize the sensitivity, the sensor's head consists of a pappus of slender hairs with a diameter of a few tens of microns, acting as an antenna. The mechanical behavior of the sensor is described in Bruecker and Mikulich[6] as a forced system with second-order response in overdamped condition (overdamped harmonic oscillator). A calibration of the mechanical model can provide the two unknown variables of the solution to the response function, the constant gain K and the cut-off frequency f_c, the frequency at which the sensor can no longer follow the excitation. A detailed view of the sensor is shown in Fig. 2. The stem and head were taken from a nature-grown Dandelion with a pappus of radially arranged slender hairs (mean length $l = 7$ mm, mean diameter $d = 30$ μm)[6]. It has a stem height of $z_0 = 7$ mm and the overall radial diameter of the pappus is about $D_p = 14$ mm. The Reynolds number Re of the flow around the individual hairs - simplified as thin cylinders of diameter d - is of the order of $Re_d \approx 2$ for air speeds of $1\ \mathrm{ms}^{-1}$. Thus, the drag is dominated by viscous friction and it scales, therefore, approximately linear with the flow speed[8-10]. The elastic joint, at which the stem's foot is bonded, is made from rubber silicone (Polydimethylsiloxane, PDMS; Youngs modulus $E \approx 1.5$ MPa) and acts as a linear-elastic torsional spring with uniform bending stiffness in radial direction. When the stem with the pappus is exposed to an air flow parallel to the wall, the resulting torque tilts the stem around the joint, similar to an inverted pendulum. As the tilt is proportional to the torque, the latter can be measured indirectly by the end-to-end shift vector $\vec{Q}(t)$ of the tip relative to the wind-off reference. We capture the tilting motion of the pappus by imaging it's orbital motion from top, which provides the projection of the tip's end-to-end vector in the horizontal x, y plane at $z = z_0$ with $\vec{Q}_{x,y}(t) = [Q_x(t), Q_y(t)]$. For small tilt angles and a sufficiently small sensor scale with $z_0 \ll \delta$, these quantities are directly proportional to the wall shear stress components $\tau_{x,y}$ (see also in Skupsch et al.[11]). In 3D flows the wall shear stress is a vector $\vec{\tau}(t) = [\tau_x(t), \tau_y(t)]$, respectively the streamwise and the spanwise component (assuming the mean flow parallel to the wall in x-direction). Both components are defined by the wall-normal velocity gradients $\partial u_x/\partial z|_{z=0\mathrm{mm}}$ and $\partial u_y/\partial z|_{z=0\mathrm{mm}}$ at the wall (in the plane perpendicular to the wall-normal coordinate z). Using a Taylor expansion, the information of the velocity field in the x, y plane close to the wall at a distance $z = z_0$ is related to the wall shear stress as follows[12]:

$$\tau_{x,y} = \mu \frac{u_{x,y}(z_0)}{z_0} + O(z_0)^2 \qquad (1)$$

with

$$u_{x,y}(z_0) \approx K Q_{x,y} \qquad (2)$$

The second order term in Eq. 1 can be neglected in the viscous-dominated near-wall region (viscous sublayer). Previous flow studies in the BOI using Laser Doppler Velocimetry show a typical profile of the mean velocity at the position of the sensor, measured using Laser Doppler Velocimetry, see Fig. 1. The linear part of the profile as indicated by the dashed line represents the viscous sublayer close to the wall. The picture additionally displays a true-scale sketch of the sensor, which illustrates that the sensor is at the edge of the linear regime. Measurements by Ampofo and Karayiannis[16] in a similar low-turbulence convection flow as studied herein show that the viscous sublayer thickness is of order of 10 % of the outer boundary layer, similar as observed in the BOI. The constant gain K in Eq. 2 was measured in-situ using a wind-generating device placed inside the BOI under isothermal conditions (see Fig. 3). The air flow is generated with a planar nozzle that generates a Blasius-type wall-jet at the location of the sensor 20 slot heights h_s away (Brücker & Mikulich 2017). Different jet velocities up to $v = 1.50\ \mathrm{ms}^{-1}$ have been set and the deflection $\vec{Q}_{x,y}$ of the sensor head was measured.

The results of the calibration procedure show a proportional increase of $\vec{Q}_{x,y}$ with the velocity of the Blasius jet at z_0. Recalling that a linear relationship is expected between air velocity and pappus drag a linear regression is applied to the measurements for the interesting range of velocities < 0.8m/s, which provides the gain $K = 1000\ s^{-1}$ with the standard error of 5%.

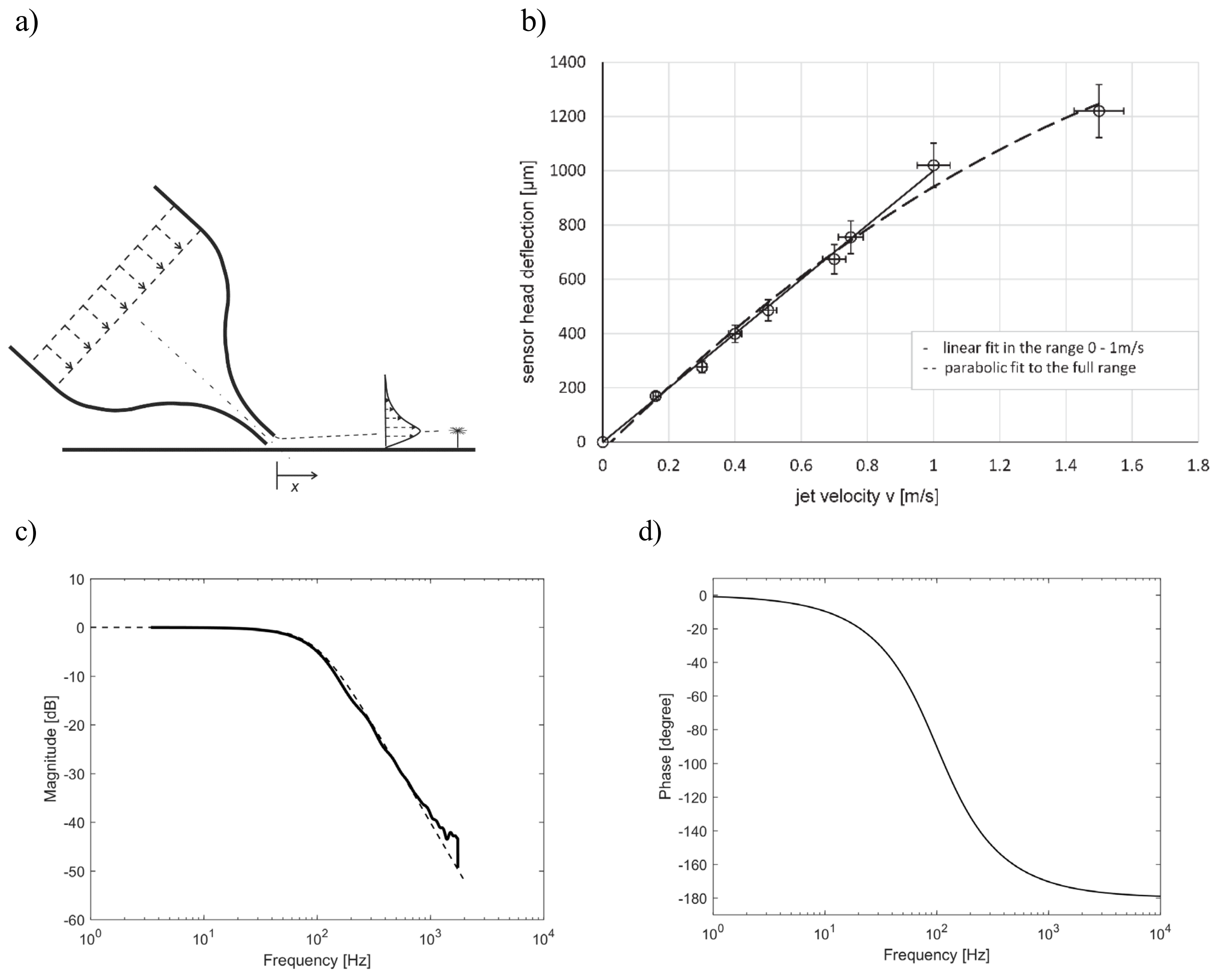

Figure 3: Sketch of the wall-jet apparaturs a) for static sensor calibration shown in b). The dynamic response was measured with a step-response test with the magnitude and phase given in c) and d), respectively. The dashed line in c) indicates the theoretical response of a second-order critically damped system fitted to the measured parameters

Beyond a velocity of about 0.8 ms^{-1}, the recordings show that the configuration of the hairs starts to change over time and the linear relationship is no longer valid. This critical value is never exceeded in the convective airflow in the BOI. A step-response test with the sensor further provides the dynamic response, given as the magnitude and phase of the transfer function, see Fig. 3c and 3d. The curves match the response of a second-order critically damped mechanical oscillator from which one obtains the cut-off frequency f_c, at which the sensor can no longer follow the signal (the response starts to roll-off at -40 dB per decade). This is at a frequency of 100 Hz, which alternatively means a response time of approximately about $\tau_{95} = 10$ ms in reverse. Since the typical time-scale of the smallest near-wall fluctuations has been measured in the past with about 0.5 s[15], the sensor works completely in the range of constant amplitude response (gain) and zero phase-shift in the measurement range of $f < 2$Hz, capable to map the full dynamics of the flow.

B. Optical set-up for sensor imaging

The optical set-up for the tip-deflection measurements is shown in Fig. 1. The pappus sensor at the bottom plate was illuminated by a defocused Laser beam (Raypower 5000, 5~W power at $\lambda = 532$ nm, Dantec Dynamics, Skovlunde, Denmark) expanded to illuminate a spot of 50 mm diameter at the floor. A CCD camera (mvBlueFOX3-1031, Matrix Vision, Oppenweiler, Germany) placed on top of the cooling plate acquires the deflection of the sensor head in the wall-parallel x, y plane with a resolution of 2048 x 1536 px^2 and a frame rate of 10 Hz. The camera is equipped with a long-distance microscope (model K2/SC™, Infinity Photo-Optical, Goettingen, Germany), which provides a resolution of 185 px/mm. A total number of 54,000 images was recorded in a single measurement campaign. The images are streamed via USB~3 to the hard disc of a desktop. This equates to a maximum of 1.5~hours of observation time per experiment. To avoid any vibrations during the recordings, the facility was left alone after starting the recording and no external disturbance could enter the RB cell. In order to remove any vibration induced by leaving and re-entering the facility, the first and the last 2-3 minutes were rejected before we analysed the data.

The tip displacement vector in the images is obtained using a 2-D cross-correlation method similar as in Particle Image Velocimetry technique[17], where we compare the quadratic subsection of the sensor image between wind-off and wind-on situation. The shift in tip position relative to wind-off is determined with subpixel accuracy using a 3-point Gaussian fit of the correlation peak in x- and y-direction, which has an uncertainty of about 0.05 px. A reference marker on the floor is used to correct for potential vibrations of the camera during the recordings. After multiplication of the shift with the lens magnification, the vector $\vec{Q}_{x,y}(t)$ of the sensor head is recovered for each time-step in the image sequence.

In order to make our data comparable with velocity-gradient data recently obtained from PIV measurements, we consider in the following the viscosity-divided WSS $\tau_{x,y}/\mu$ (known as the wall-shear rate) with the two components:

$$\tau_x(t)/\mu = KQ_x(t)/z_0$$

$$\tau_y(t)/\mu = KQ_y(t)/z_0 \qquad (3)$$

and we define the direction and the magnitude of the WSS as follows:

$$\Phi(t) = \mathrm{atan}(\tau_y(t)/\tau_x(t))$$

$$\Psi(t) = \frac{1}{\mu}\|\tau\| = \frac{1}{\mu}\sqrt{\tau_x^2(t) + \tau_y^2(t)} \qquad (4)$$

We capture our data with a sampling frequency of 10 Hz. In order to remove outliers, the data was filtered in time with a fourth-order Butterworth low-pass filter designed with a -3 dB cutoff frequency at 2 Hz. We have selected this particular frequency, since the typical time-scale of the smallest near-wall fluctuations has been measured in the past with about 0.5 s[15]. Our long-term recording of totally 54,000 samples covers more than 100 LSC turnover times T_e, and ensures sufficient statistical evidence even for the long timescales.

III. Results and Discussion

Preceding the discussion, it is worth to note that earlier studies in the barrel with a similar aspect ratio indicate the existence of only a single LSC roller, which was observed also to perform angular oscillations around a mean direction. The normal flow mode present in the BOI is where the mean orientation of the LSC is locked in one particular direction. Because of the modulation effect, which the outer flow enforces on the signal on the floor, the WSS signals should also reveal the footprint of this wiggling motion. Fig. 4a and b show the complete time trace of the direction $\Phi(\mathrm{t})$ and the magnitude $\Psi(\mathrm{t})$ of the WSS (viscosity-divided WSS $\tau_{x,y}/\mu$) over a period of 1.5 hours. Overlaid in color is the low-pass filtered data $\widetilde{\Phi}_{LSC}$ and $\widetilde{\Psi}_{LSC}$ (4th order Butterworth low-pass filter designed with a -3 dB cut-off frequency at 0.003 Hz), based on the notation used in Shi et al.[18] Therefore, turbulent events happening close to the wall are filtered out (higher frequency) while the footprint of fluctuations of the mean wind direction and magnitude of the LSC remain.

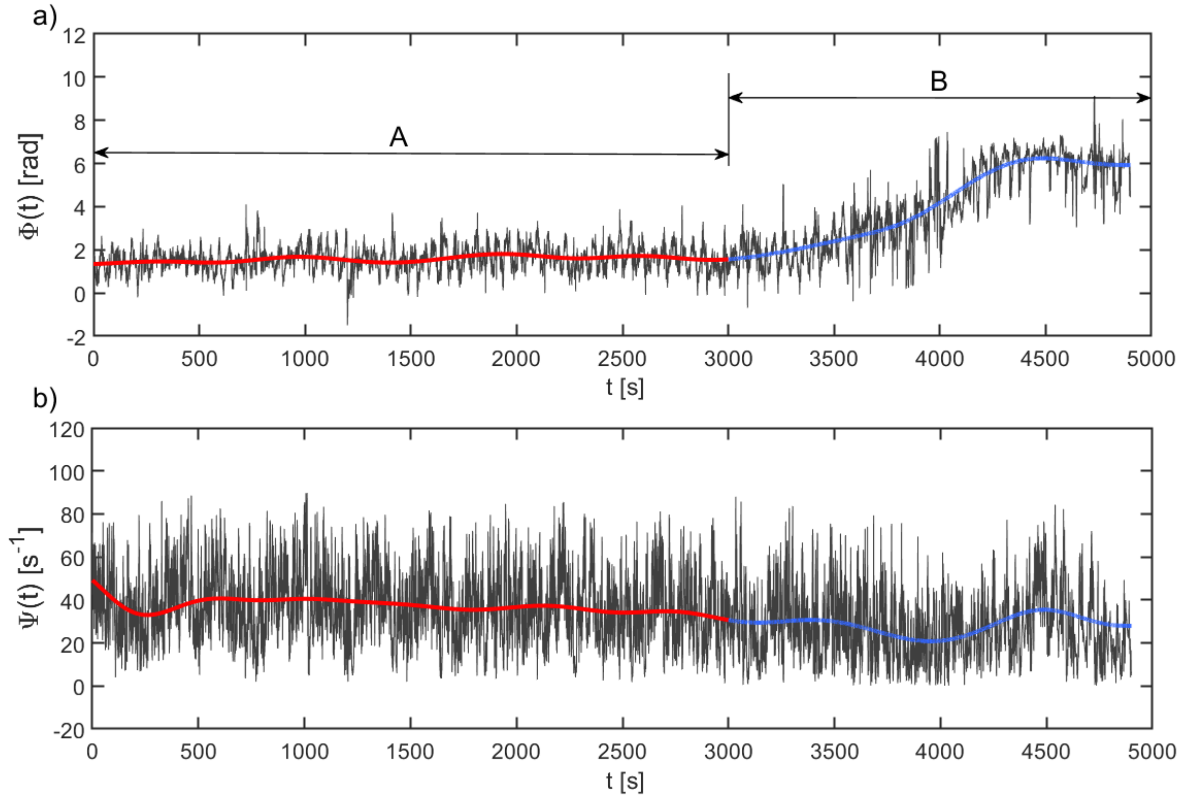

Figure 4: a) Plot of direction $\Phi(t)$ and b) magnitude $\Psi(t)$ of τ/μ over a period of 1.5 hours. Overlaid in color is the profile of the time-filtered signal of the direction $\widetilde{\Phi}(t)$ and the magnitude $\widetilde{\Psi}(t)$. Two different characteristic phases are coded in color (phase A in red, phase B in blue).

Both of the original data, the direction $\Phi(\mathrm{t})$ and magnitude $\Psi(\mathrm{t})$ of the WSS vector, fluctuate over time at a high frequency. Meanwhile, the low-pass filtered WSS vector is almost perfectly aligned with the x-axis in phase A ($t = 0 \ldots 3{,}000$ s). Beginning at $t = 3{,}000$ s, a phase of a very slow drift of the angle $\widetilde{\Phi}_{LSC}$ in counter-clockwise direction is seen, see phase B ($t = 3{,}000 \ldots 5{,}000$ s). This angular drift indicates a slow precession of the mean axis of the LSC, meanwhile the oscillations at higher frequencies persisted. Such a slow precession mode can replace the normal flow mode present in the BOI. Initially, at $t = 1{,}000$ s in phase A, the mean WSS magnitude amounts to $\overline{\Psi} = 40\ \mathrm{s}^{-1}$. It decreases then slowly over a period of $2{,}000$ s further down to $\overline{\Psi} = 30\ \mathrm{s}^{-1}$ at the end of Phase A

$(= 3000\ \mathrm{s})$ and finally reaches, in a rather short period, a minimum of $\overline{\Psi} = 20\ \mathrm{s}^{-1}$ at $t = 4{,}000\ \mathrm{s}$ in phase B (see Fig. 4b). The final slow-down lasted only about 1,000 s (366 units of T_f), which is when the angle $\widetilde{\Phi}_{LSC}$ changed by π. Fig. 5 illustrates the complex behaviour of the flow in the x, y plane as a trace plot of the original and low-pass filtered WSS vector. As discussed before, the mean direction of the LSC in phase A (the red part of the time-filtered signal in Fig. 4) was almost constant towards north (positive x-axis), while in phase B the plane of the LSC shows a nearly constant angular drift in counter-clockwise direction.

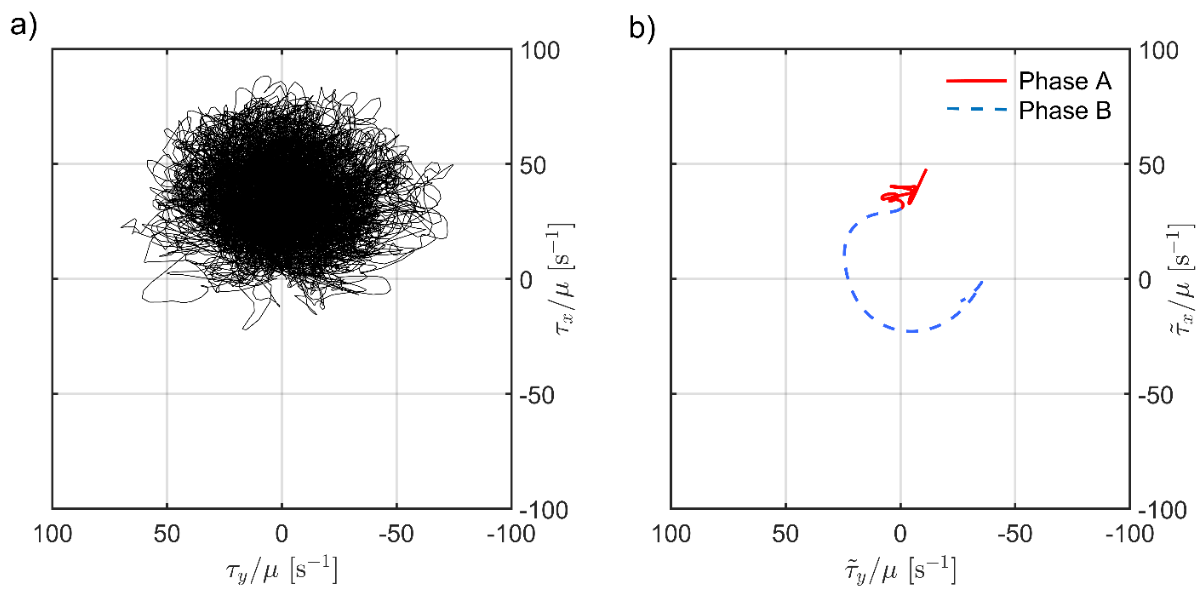

Figure 5: Time trace of the viscosity-divided WSS vector $\tau/\mu(t)$ in the x, y plane, comparable to the trace $Q(t)$ of the sensor head. a) $\tau/\mu(t)$ in phase A; b) time-filtered signal $\tilde{\tau}/\mu(t)$ in phase A (full red line) and in the successive phase B (dashed blue line).

When correlating the onset of the angular drift with the magnitude of the WSS, the data let us conclude that the mean axis of the LSC started to rotate at a time, when the magnitude of the main wind started to critically slow down. If we again follow the argument of the outer modulation effect, then the magnitude of the low-pass filtered WSS is proportional to the characteristic velocity of the LSC (mean wind). From that, we can estimate the kinetic Energy $\bar{E}_{kin}$ of the LSC as proportional to the square of the magnitude of the WSS with $\bar{E}_{kin} \sim \Psi^2$. The results show therefore that the average kinetic energy of the mean wind in phase B is reduced to about 50 % of the energy in phase A. Such a slow-down was also observed by du Puits et al.[7] We hypothesize herein that the slow-down of the kinetic energy of the mean wind may have triggered the angular precession. The time scale of this precession is rather long, as it takes about 20 characteristic eddy turnovers of the LSC while the orientation drifts only along an angular arc of π.

We further analyze the temporal behavior of the magnitude Ψ and the angle Φ by computing their autocorrelation functions:

$$C_{xx}(\Delta t) = \lim_{n \to \infty} \frac{1}{n} \sum_{i=1}^{n} x_i(t) x_i(t + \Delta t) \qquad (5).$$

We plot short in Fig. 6a and b exemplary short sequences of the time traces of $\Psi(t)$ and $\Phi(t)$ together with the autocorrelation functions $C_{xx}(\Psi)$ and $C_{xx}(\Phi)$ calculated from the full data. While the oscillations of the magnitude $\Psi(t)$ seem to be rather irregular (see Fig. 6a), the plot of $\Phi(t)$ reveals a low frequency oscillation around the mean with a frequency of about 0.02 Hz (see Fig. 6b). This oscillatory variation of the orientation of the WSS angle $\Phi(\mathrm{t})$ over a range of more than ±25 degrees is similar as already observed in Shi et al.[18]. The timescale related to this oscillation corresponds to the characteristic turnover time $T_e \approx 50$ s of the LSC. Its quasi-periodic nature is highlighted in the plot of the autocorrelation function $C_{xx}(\Phi)$ (see Fig. 6d), which shows strong periodic correlation peaks at multiples of the time-lag T_e(Fig. 6d). The dynamical system has obviously two attracting states in the orientation of the LSC overlaid with a certain fraction of noise/turbulence.[20]

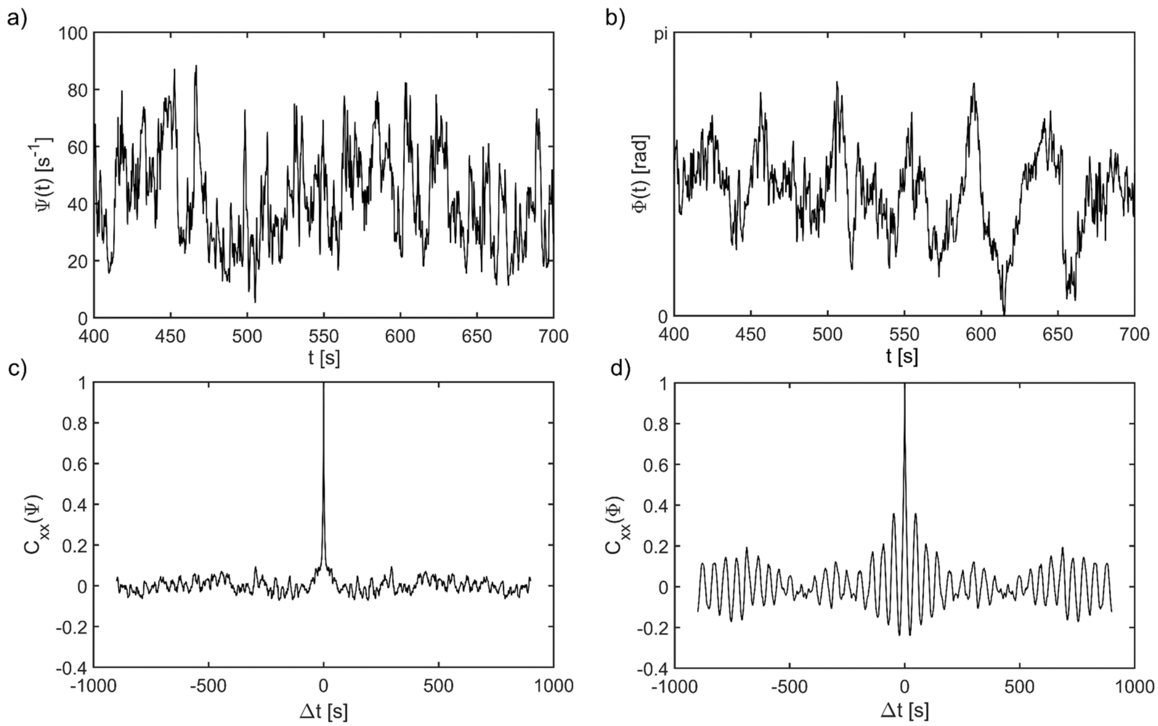

Figure 6: a,b) Time series of magnitude $\Psi(t)$ and direction $\Phi(t)$ of the wall shear stress vector τ/μ for phase A, $400\ s < t < 700\ s$; c,d) autocorrelation function of the magnitude $C_{xx}(\Psi)$ and the direction $C_{xx}(\Phi)$ for phase A.

Furthermore, the result shows a long-term modulation of the angular oscillations. The peak amplitude of the correlation slowly decreases for increasing time lag to about zero at a time lag of $\Delta t =$ 450 s (corresponds to $9T_e$) and then increases again to a local peak correlation value $C_{xx}(\Phi) = 0.2$ at $\Delta t = 700$ s ($14T_e$). The observed slow-down of the mean wind in phase B could be a consequence of this low-frequency modulation.

In the following, we exclusively focus on phase A when the mean direction of the wind is constant on a large time-scale and aligned with the x-axis with a mean WSS magnitude of $|\tau_{x,}|/\mu = 35\ s^{-1}$ and a rms of $\tau'_{x,rms}/\mu = 18.3\ s^{-1}$. An interesting feature is the observation of a negative streamwise wall shear stress τ_x as seen in the traces in Fig. 5a, when the line crosses the 2nd or 3rd quadrant in the left sub-figure. Such events are observed in turbulent RB convection for the first time, but they were observed recently in turbulent boundary layer flows[4].

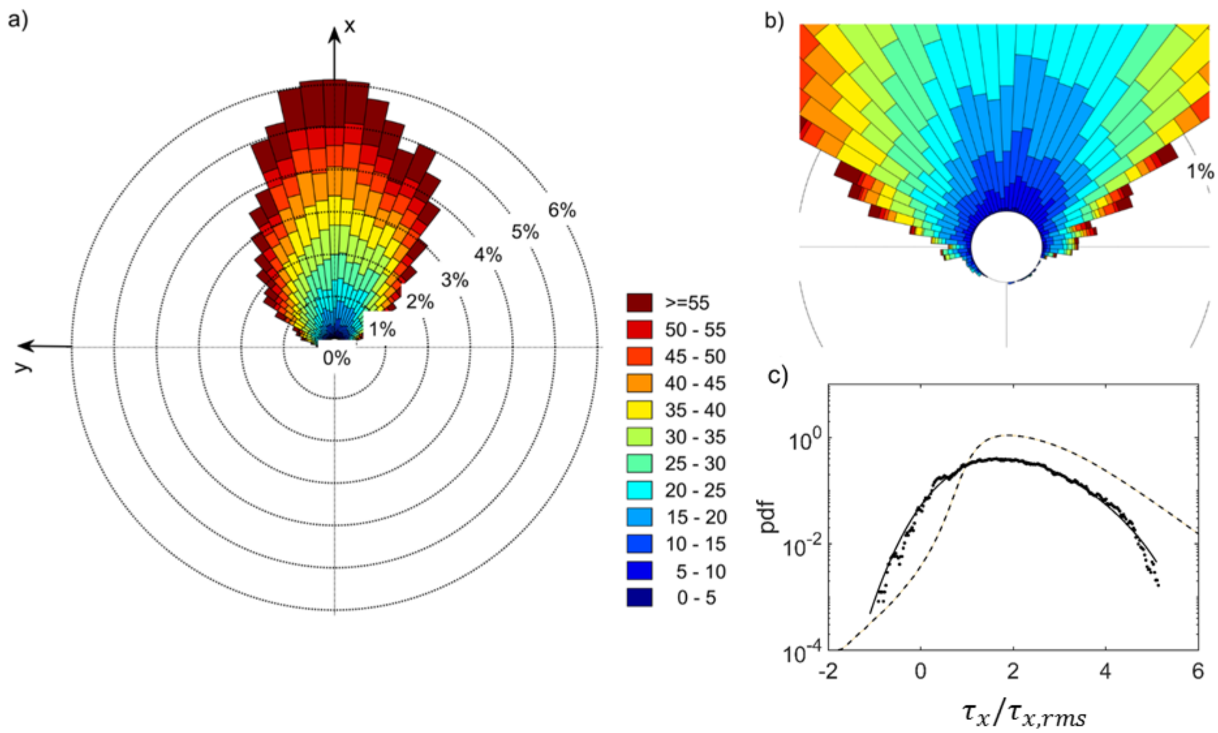

Figure 7: a) Polar plot of probability distribution of the wall-shear angle in phase A (mean wind flow is in x-direction). b) Zoom-in the image of the data given left. Angular steps are in 5 degrees. The color indicates the magnitude in the ranges given in the legend bar. c) Pdf of the streamwise wall shear stress normalized with its rms. The solid line represents the generalized extreme value distribution according to Eq. 6 and with the parameters given in the text. The dashed line shows the results from Örlü & Schlatter (2011) for a zero pressure-gradient turbulent boundary layer flow [25].

Fig. 7 shows the angular probability density function of the yaw angle of the WSS as a wind rose plate with a mean direction towards north (x-axis). The angle Φ of the rays relative to north represent the yaw angle, while the length indicates the probability over all samples recorded in phase A. The magnitude Ψ is overlaid in colour. The graph is similar to that used by Bruecker displaying the measurements of the statistics of the wall shear stress in turbulent boundary layer (tbl) flows[4]. The distribution shows a type of cone, in which mean angles between ±25 degrees around the x-axis predominate. However, there are also, even rarely, events of τ, in which the yaw angle exceeds ±90 degrees. Thus, these rare events can be associated with events of large spanwise τ_y, first argued in a zero-pressure-gradient tbl[4]. The probability and the yaw angle of the rare events in thermal convection are quite similar to those reported from tbl measurements. It however remains open if the origin of such events is the existence of quasi-streamwise vortices as argued in the case of tbl. The observation herein indicates a rapid temporal variation of the local direction of the fluctuating wall shear stress, representing a high angular velocity of the WSS vector τ during these events. Fig 7c shows the pdf of the streamwise WSS normalized with the rms. It demonstrates a non-symmetric distribution with prove of certain probability of negative streamwise WSS events. The measured PDFs shown in Fig. 7c can be well described by the generalized extreme value (GEV) distribution[19].

$$P(x';\lambda,k) = \frac{1}{\lambda}(1+kx')^{-(1/k+1)}\, e^{-(1+kx')^{-1/k}} \tag{6}$$

where the variable $x' = (x-m)/\lambda$ with the shape parameter k, the scale parameter λ, and the location parameter m. The fit provides a shape parameter of $k = -0.1907$ ($\lambda = 0.937$, $m = 1.5403$). For $k < 0$, the distribution is reduced to the reversed Weibull distribution and has zero probability density for $x > -\lambda/(k+m)$. From the fitted values of x, we find the corresponding upper bound with x > 6.4553. Note that the herein observed distribution is reverse to the typical Weibull-type distribution observed in tbl, see the reference curve in Fig. 7c from Örlü & Schlatter (2011) [25]. This means negative streamwise WSS events can have higher magnitude in convection flows.

With respect to the occurrence of extreme events, it is quite difficult to analyse the data using classical conditional averaging methods or a fixed threshold definition due to this particular modulation of the magnitude and the orientation of the mean flow. Here, we try to discriminate the amplitude of the fluctuating WSS signals into separate timescales. We distinguish between the periodic transitive dynamics represented in the low frequency dynamics of the mean wind and the small-scale turbulent fluctuations. To this end, we apply envelope functions with different time windows on τ_x to determine the amplitudes of these fluctuations on the different timescales. The envelope is calculated from the Matlab toolbox and uses a sliding time-window that connects within the window the local peaks (upper envelope for local maxima and lower envelope for local minimum peaks) with a smoothed spline[21].

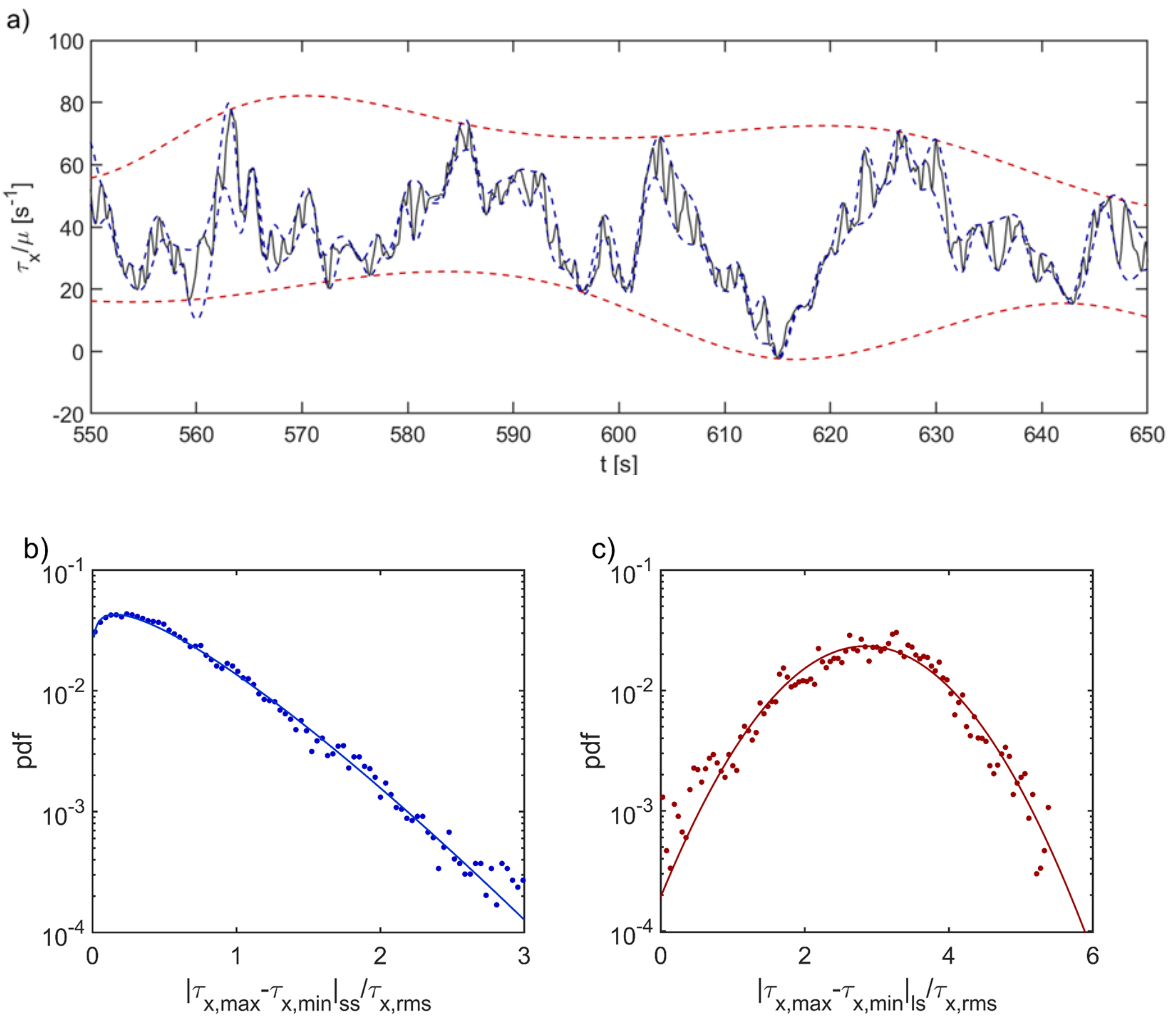

Figure 8: Peak-to-peak amplitude of the fluctuations of τ_x at different timescales. a) Time trace of τ_x (black line) with envelopes of the small-scale (ss) and large-scale (ls) fluctuations (thin blue and red lines, respectively). b) Probability density function (PDF) of the small-scale fluctuations (the solid line is a Weibull fit with a scale parameter $\lambda = 0.673$ and a shape parameter $k = 1.223$, c) PDF of the large-scale fluctuations (the solid line is a Gaussian fit with a mean value of $\bar{\tau}_x = 2.85$ and a standard deviation of $\sigma(\tau_x) = 0.92$)

For the low frequency dynamics, we chose a window of 15 s, while using a shorter time window of 0.5 s for the small-scale turbulent structures. One typical example of such an enveloping curve is plotted along with the original signal in Fig. 8a. In order to analyze the amplitude of the fluctuations, we compute the absolute difference between the upper and the lower envelopes$|\tau_{x,max} - \tau_{x,min}|$ and determine the probability density function (PDF) for both time windows (see Figs. 8b and c). The PDF of the small-scale (ss) fluctuations using a time window of 0.5~s is shown in Fig. 8b, that for the large-scale (ls) fluctuations is shown in Fig. 8c. While the ss fluctuations of the streamwise wall shear stress follow a Weibull distribution according to:

$$P(x; \lambda, k) = \frac{k}{\lambda}\left(\frac{x}{k}\right)^{k-1} e^{-(x/\lambda)^k} \tag{7}$$

(with the scale parameter $\lambda = 0.637$ and the shape parameter $k = 1.223$), the ls fluctuations are clearly Gaussian distributed. The latter indicates a normal distribution of the amplitude of the angular fluctuations of the orientation of the LSC, as this contributes to the cyclic variation of τ_x. In conclusion, extreme events are more likely, if large excursions occur simultaneous for both statistical distributions.

IV. Conclusion

We have presented and discussed the first measurements of the instantaneous wall shear stress in a large-scale Rayleigh-Bénard experiment at Rayleigh and Prandtl numbers $Ra = 1.58 \cdot 10^{10}$ and $Pr = 0.7$, respectively. Using a novel, nature-inspired pappus sensor, we measured the magnitude and the orientation of the local wall shear stress vector at the center of the heated bottom plate. The results of our 1,5 hours measurement series demonstrate that this vector undergoes strong fluctuations as well in its magnitude as in its orientation. Important to note is that the sensor signal at the wall represents the sum of both, the fluctuations on small time-scales due to the turbulent nature of the boundary layer, and in addition the dynamics of the LSC due to the modulation effect of the outer flow onto the near-wall region. Therefore, our measurements allow also drawing conclusions on the magnitude and orientation of the main wind in the LSC. On average over a period of 3000s (phase A), the mean wind is almost perfectly aligned with the x-axis. However, we observe a clear quasi-periodic angular precession of the orientation of the LSC in the range 50-60° around the mean, each half-cycle taking exactly the time of one eddy turn-over time $T_e \approx 50\,\mathrm{s}$. The strong periodicity is manifested by the plot of the autocorrelation function $C_{xx}(\Phi)$, which shows periodic peaks at multiples of the eddy turn-over times with values larger than 0.2 even after more than 900 s (see Fig. 6d). Such a strong periodicity in the angular oscillations has not been observed so far and motivated us to illustrate the dynamics of the LSC in a simplified mechanical model for further discussion.

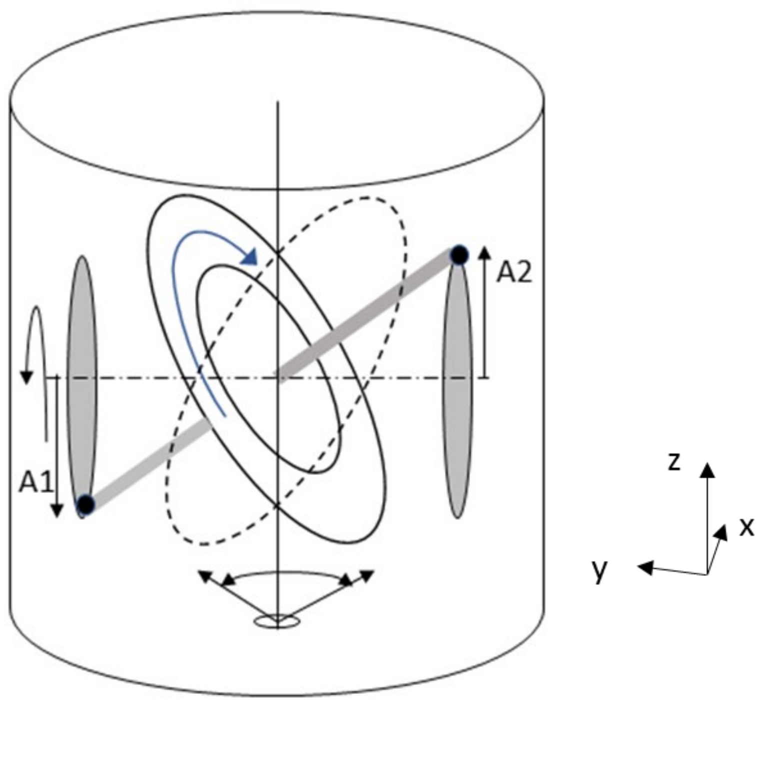

Figure 9: Simplified mechanical model of a tumbling rotating disc (tumbling LSC) to illustrate the modulation

effect on the quasi-periodic angular precession of the wall shear stress vector at the wall

A schematic mechanical model is illustrated in Fig. 9 to discuss the observed regular oscillations. We hypothesize that the plane of the LSC with fluid rotating around its axis is represented by a rotating disc, which axis is initially aligned horizontally with the y-axis. An initial disturbance in form of asymmetric lateral down- and upwash at the sides of the LSC (A1-A2) cause a torque which tilts the spin momentum of the LSC in the horizontal plane and leads to a self-enforcing of this asymmetry. As the vortex axis reorients away from the horizontal plane, it generates a torque around the z-axis because of conservation of angular momentum, which leads to a precession of the LSC. The cycle is reversed when the front of the LSC – while precessing - reaches the region A2 and counteracts the upwash, while the back of the LSC reverses the downwash A1. Hence, the system starts a cyclic clock-wise – counter-clock wise precession motion around the z-axis, which correlates with the observed regular angular oscillations of the orientation of the WSS vector. Note that the diagonal orientation of the LSC is not contradicting previous observations that the orientation of the mean flow at the same instant and location is different at the bottom plate compared to the top plate, supporting the idea of a tilted or twisted circulation roll (Funfschilling & Ahlers 2004 [23] ; Xi & Xia 2008 [24]).

The long-term recording also allowed us to detect a very slow drift of the mean orientation in a certain phase (phase B) overlaid with the regular precessions described above. The angular drift in counter-clockwise direction takes about 30 times the eddy turn-over time for a 270° turn. This slow mode is accompanied by a decrease of the kinetic energy of the mean wind (imposed by the LSC) by about 50 %. In the past, du Puits et al. reported at similar conditions also a critical weakening of the mean wind for a period of four hours[22]. However, the authors could not link their observation to a modification of the angular orientation of the global recirculation. A possible explanation for this slow mode precession based on the proposed mechanical model could be a slight imbalance of the tumbling cycle, which then leads to a net mean angular momentum. Transitional flow phenomena like the reported rotation of the plane of the global recirculation has already been observed in turbulent Rayleigh-Bénard convection (RBC) in the past, see [23,24]. However, they found that occur only very rarely. Insofar, it was rather a lucky coincidence that we could observe such a transition in our 90 minutes long measurement.

Another phenomenon we observed in our long-term recordings is the occurrence of local backflow in the boundary layer, while the large-scale circulation in phase A remains on average almost perfectly aligned with the x-axis. Such local backflow events have also been detected recently in turbulent boundary layer flow along a flat wall, but this is the first time that such events could be documented in a temperature-gradient driven flow. Local backflow is correlated herein with large angular velocities of the wall shear stress vector, which we understand as an indication for the existence of coherent vortical structures with a large inclination of the axes against the wall (nearly wall-normal vortex funnels). These short-term fluctuations have amplitudes which follow a highly skewed Weibull distribution, while the amplitudes of fluctuations on the longer time scales are better fitted by a symmetric Gaussian. In both distributions, the ends of the tails can reach amplitudes of 3-4 times the rms of the mean streamwise wall shear stress. Such a coincidence of large values in both distributions indicates the high probability of rare excursions of the near-wall flow, in magnitude as well in yaw angle.

ACKNOWLEDGEMENTS

The position of Professor Christoph Bruecker is co-funded as the BAE SYSTEMS Sir Richard Olver Chair and the Royal Academy of Engineering Chair (grant RCSRF1617/4/11) which is gratefully acknowledged. We wish to acknowledge the support of the European Union under the Grant Agreement number 312778 as well as the support from the German Research Foundation under the grant number PU436/1-2 (the camera was sponsored in grant BR 1491/30-1). Moreover, we thank Vladimir Mikulich, Sabine Abawi, and Vigimantas Mitschunas for their technical assistance to run the experiment.

DATA AVAILABILITY STATEMENTS

Raw data were generated at the Ilmenau Barrel large-scale facility. Derived data supporting the findings of this study are available from the corresponding author upon reasonable request.

REFERENCES

[1] L. Prandtl, “Bericht ueber Untersuchungen zur ausgebildeten Turbulenz,“ Z. angew. Math. Mech. 5, 136 (1925).

[2] H. Ludwieg, “Bestimmung des Verhaeltnisses der Austauschkoeffizienten fuer Waerme und Impuls bei turbulenten Grenzschichten, Z f. Flugwiss. 4, 73 (1956).

[3] J. D. Scheel, J. Schumacher, “Local boundary layer scales in turbulent Rayleigh-Bénard convection,” J. Fluid Mech. 758**,** 344 (2014).

[4] C. Bruecker, “Evidence of rare backflow and skin-friction critical points in near-wall turbulence using micropillar imaging,” Phys. Fluids 27, 031705 (2015).

[5] V. Bandaru, A: Kolchinskaya, K. Padberg-Gehle, J. Schumacher, "Role of critical points of the skin friction field in formation of plumes in thermal convection," Phys. Rev. E 92, 043006 (2015).

[6] C. Bruecker. V. Mikulich, "Sensing of minute airflow motions near walls using pappus-type nature-inspired sensors," PLoS ONE 12, e0179253 (2017).

[7] R. du Puits, C. Resagk, A. Thess, "Structure of viscous boundary layers in turbulent Rayleigh-Bénard convection," New Journal of Physics 15, 013040 (2013).

[8] E. Liebe, *Flow Phenomena in nature. A challenge to engineering design* (Wit Press/Computational Mechanics, Southampton, 2006).

[9] C. Pandolfi, D. Izzo, "Biomimetics on seed dispersal: survey and insights for space exploration," Bioinspir. Biomim. 8, 025003 (2013).

[10] V. Casseau, G. De Croon, D. Izzo, C. Pandolfi, "Morphologic and aerodynamic considerations regarding the plumed seeds of tragopogon pratensis and their implications for seed dispersal," PLOS ONE 10, 1 (2015).

[11] C. Skupsch, M. Sastuba, and C. Bruecker, "Real time visualization and analysis of sensory hair arrays using fast image processing and proper orthogonal decomposition," 17th International Symposium on Applications of Laser Techniques to Fluid Mechanics (Lisbon, Portugal, 2014).

[12] C. Bruecker, D. Bauer, H. Chaves, "Dynamic response of micro-pillar sensors measuring fluctuating wall-shear-stress," Exp. Fluids 42, 737 (2007).

[13] O. Levin, V. G. Chernoray, L. Loefdahl, D. S. Henningson, "A study of the blasius wall jet," J. Fluid Mech. 539, 313 (2005).

[14] C. Resagk, R. du Puits, A. Thess, F. V. Dolzhansky, S. Grossmann, F. F. Araujo, D. Lohse, "Oscillations of the large scale wind in turbulent thermal convection," Phys. Fluids 18, 095105

(2006).

[15] R. du Puits, C. Resagk, A. Thess, "Breakdown of wind in turbulent thermal convection," Phys. Rev. E 75, 016302 (2007).

[16] F. Ampofo and T. Karayiannis, "Experimental benchmark data for turbulent natural convection in an air filled square cavity," Int. J. Heat Mass Transf. 46, 3551 (2003).

[17] M. Raffel, C. E. Willert, S. Werely, J. Kompenhans, *Particle Image Velocimetry. A Practical Guide* (Springer, Berlin Heidelberg, 2007).

[18] N. Shi, M. S. Emran, J. Schumacher, "Boundary layer structure in turbulent Rayleigh-Bénard convection," J. Fluid Mech. 706, 5 (2012).

[19] S. Kotz and S. Nadarajah, *Extreme Value Distributions Theory and Applications* (Imperial College Press, London, 2000).

[20] U. A. Kumar, A. Durga, "Application of extreme value theory in commodity markets," Proc. of the IEEE International Conference on Industrial Engineering and Engineering Management 867 (2013).

[21] MATLAB, version 9.0.0.341360 (R2016a) The MathWorks Inc., Natick, Massachusetts.

[22] R. du Puits, C. Resagk, A. Thess, "Mean Velocity Profile in Confined Turbulent Convection," Phys. Rev. Lett. 99, 234504 (2007).

[23] D. Funfschilling, G. Ahlers, "Plume motion and large-scale circulation in a cylindrical Rayleigh–B´enard cell," Phys. Rev. Lett. 92, 194502 (2004).

[24] H. D. Xi, K. Q. Xia, "Azimuthal motion, reorientation, cessation, and reversal of the large-scale circulation in turbulent thermal convection: a comparative study in aspect ratio one and one-half geometries," Phys. Rev. E 78, 036326 (2008).

[25] R. Örlü, P. Schlatter, "On the fluctuating wall-shear stress in zero pressure-gradient turbulent boundary layer flows,". Phys. Fluids 23, 021704 (2011).